Acta Materialia 260 (2023) 119333

Contents lists available at ScienceDirect

Acta Materialia

journal homepage: www.elsevier.com/locate/actamat

Full length article

Metrics for the characteristic length scale in the random bicontinuous microstructure of nanoporous gold

Sambit Bapari [a,*], Lukas Lührs [a], Jörg Weissmüller [a,b]

[a] Institute of Materials Physics and Technology, Hamburg University of Technology, 21073 Hamburg, Germany
[b] Institute of Materials Mechanics, Helmholtz-Zentrum Hereon, 21502 Geesthacht, Germany

ARTICLE INFO

Keywords:
Nanoporous
Ligament size
Surface area
Microstructure
Heterogeneity

ABSTRACT

Nanoporous gold (NPG) made by dealloying exemplifies materials with random bicontinuous microstructures that can be approximated by leveled-wave type models. As a distinguishing feature, the characteristic length scale – often quantified by the "ligament size" L – of NPG may be tuned over several orders of magnitude while the microstructural geometry retains a high degree of self-similarity. It is therefore essential to have at hand accurate procedures for determining the size by experiment and to match it to analogous size metrics of model scenarios. Working with a set of NPG samples of widely different size, we compare ligament size distributions determined by analysis of scanning electron micrographs to those of the leveled-wave model. The model is representative of various material types with random bicontinuous microstructures. The size distribution is remarkably uniform over the cross-section of experimental samples. Furthermore, the distribution evolves self-similarly upon coarsening, and the normalized distribution width agrees closely to that of the model. A measure for size determined by the electrochemical capacitance ratio method correlates well with L. This supports a protocol for converting between the two measures. As a dimensionless factor characteristic of the microstructural geometry of random dual phase microstructures, the product of L and the specific surface area is found consistent between experiment and model. The findings suggest conversion factors between the various metrics, and they advertise the combination of NPG and the leveled-wave model as a showcase for characterizing the characteristic length scale of random bicontinuous microstructures.

1. Introduction

Nanoporous gold (NPG) made by dealloying exhibits a bicontinuous microstructure, in which the characteristic length scales can be tuned between few nanometers and micrometers [1–3]. The material is distinguished by its structural uniformity and definition, and by the reproducibility of its preparation [4,5]. Thereby, it provides a showcase and a convenient model system for random network materials. The microstructure of such materials exhibits a substantial complexity. A recent review [6] advertises phase fraction, connectivity, tortuosity, surface curvature, grain size and chemical heterogeneity as descriptors which are each relevant for distinct aspects of the materials behavior. Given 3D reconstructions, even more (and more complex) aspects of the microstructure may be accessible and serve for classification — these include Minkowski functionals [7], principal curvature correlations [8] and ring structures of graph theory [9]. Yet, by far the most prominent descriptor of the NPG microstructure is its characteristic length scale.

Length scales are of particular relevance for NPG, since functional [10–14] and mechanical [15–18] properties are substantially dependent on the specific surface area or on the size of the ligaments. Not surprisingly, the ligament size is reported in most studies in the field. Yet, not every study uses the same metric for size. This raises the question, how can sizes reported in different studies be compared?

The just mentioned question is rarely addressed, and conversion schemes have not in all instances been established. This concerns specifically the comparison between the mean ligament waist diameter, L_W, as obtained from scanning electron micrographs (SEM) – the most common approach [19–24] – and an effective size, L_α, estimated as inversely proportional to the specific (per volume) surface area α. The latter parameter is accessible through various techniques, including electrochemical approaches [23,25–30], gas adsorption [26–28], and the analysis of 3D tomographic reconstructions [31–34].

Electrochemical approaches to α appear particularly attractive, since NPG is routinely prepared by corrosion in aqueous environment, often under electrochemical control. Characterizing the ligament size by electrochemical techniques is then a comparatively simple extension of the preparation approach. Furthermore, the characterization is

* Corresponding author.
E-mail address: sambit.bapari@tuhh.de (S. Bapari).

https://doi.org/10.1016/j.actamat.2023.119333
Received 8 May 2023; Received in revised form 4 September 2023; Accepted 5 September 2023
Available online 10 September 2023

nondestructive and it probes the entire NPG specimen rather than a local spot.

The electrochemical approach relies on inferring the net surface area, A, of a specimen from its net capacity, using a reference value for the area-specific capacitance or pseudo-capacitance. The reference value for capacitive double layer processes is notoriously sensitive to experimental detail and so should not be used for quantifying A in absolute numbers [35]. The value for oxygen sorption is believed to be more robust, yet oxidation/reduction cycles are known to induce coarsening and so change the very feature that is to be characterized. In fact, double layer capacitance ratio experiments are accepted for the relative comparison of area-of-surface values, provided that experimental details are meticulously kept comparable [35].

SEM data probe only a small fraction of the sample volume and this might not be representative in case there was significant macroscale heterogeneity. Furthermore, the counting statistics requires attention — how many ligaments need be analyzed for a representative average value? As an imaging approach, SEM analysis supports protocols that address these issues.

The interrelation between different size metrics of random structures depends on their microstructural morphology. Based on the morphology of early-stage spinodal microstructures, the leveled-wave model [36,37] is distinguished by matching elasticity [37], strength [38], and the reduced topological genus [33,37] of NPG with ligament size as the only free parameter [6]. The model also applies to such different materials as spinodally decomposed solid solutions, porous glasses such as vycor, as well as some microemulsions and polymer blends [39]. The structural similarity between these different materials classes, including dealloyed nanoporous metals, emphasizes the interest in NPG as a model system for random bicontinuous microstructures. Various size metrics for the leveled-wave model have been explored [37], yet the mean ligament waist diameter, as the key parameter in experiment, is not among those metrics.

Here, we explore interrelations between the various size metrics of NPG. Working with experimental samples spanning more than one order of magnitude in ligament size and with a set of leveled-wave structures generated numerically, we analyze the ligament diameter distribution based on images of the microstructure and the specific surface area based on electrochemical capacitance experiments or on closed-form solutions for the model. The excellent correlation between SEM-based ligament size and electrochemically determined specific surface area suggests an experimental protocol for the capacity-based estimate of the mean ligament diameter. We assess the results by comparison with the ligament diameter distribution of the leveled-wave model. Our analysis of that model extends the range of parameters for which the model can be linked to experiments on random network materials in general and specifically on NPG.

2. Scaling between ligament size and specific surface area

The quantities of primary interest in our study are a characteristic mean ligament size, L_W, and a (volume-) specific surface area, α. Operationally, L_W is determined based on a sample of the diameters of many ligaments at their waist in an analysis of SEM images of fracture surfaces of NPG [20]. The mean of that sample is identified with L_W. The specific surface area is defined as the net area of surface in a body of NPG, divided by the net volume of the solid phase. From the various approaches (see above) towards measuring α, our study focuses on the most commonly employed one, which is based on the electrochemical capacitance ratio method [35].

Inasmuch as the microstructure evolution of NPG during coarsening can be approximated as self-similar, the specific surface area can be expected to be inversely proportional to any measure, L, for the characteristic ligament size. In other words,

$$\alpha L = \mathfrak{C} \tag{1}$$

with the scaling factor $\mathfrak{C}$ a dimensionless constant that depends on the definition of L and on the morphology of the microstructure but is independent of its characteristic length scale.

Specifically, $\mathfrak{C}$ must be expected to vary with the solid volume fraction, φ, of NPG [27]. Practically all experimental studies of NPG have $0.2 \le \varphi \le 0.5$, and most restrict attention to the even smaller regime $0.25 \le \varphi \le 0.35$. Those restricted ranges will be emphasized in our discussion.

Geometric models for NPG suggest expectations for the numerical value of $\mathfrak{C}$. In the simplest model, the network structure of NPG is approximated as an array of monodispersed cylindrical struts. This immediately suggests $\mathfrak{C} = 4$, and in fact the estimate

$$L_\alpha = 4/\alpha \tag{2}$$

for a ligament size measure based on α is often used [25,32,40].

A more realistic representation of the microstructure of NPG is provided by the leveled-wave model. The model's α relates to its characteristic wavelength, λ, and to φ by [37]

$$\alpha = \frac{4}{\lambda\varphi\sqrt{3}}\mathrm{erf}^{-1}(2\varphi - 1)^2 . \tag{3}$$

Furthermore, interference functions of leveled-wave structures have maxima at wave number $q_0 = 2\pi/\lambda$, which implies the characteristic spacing, $\tilde{L}$, between neighboring ligaments through [37]

$$\tilde{L} = 1.23 \times 2\pi/q_0 = 1.23\lambda . \tag{4}$$

$\tilde{L}$ also manifests itself as the position, on the distance axis, of the first maximum of the microstructural autocorrelation function.

Contrary to α and $\tilde{L}$, the mean ligament diameter, L_W, at the waist in leveled-wave structures escapes a closed-form analysis. A related parameter can be obtained by an approach from granulometry [41]. To obtain this size measure, L_G, each material point in the solid phase is associated with the diameter of the largest sphere that contains the point and that fits entirely within the solid; L_G represents the mean, over all points, of that diameter. By numerical analysis of leveled-wave structures with $0.2 \le \varphi \le 0.5$, Soyarslan and coworkers found [37]

$$L_G \approx \lambda(0.53\varphi + 0.41) . \tag{5}$$

Combining Eqs. (3) and (5) with a straight-line fit in the same interval of φ, one finds that the product $\mathfrak{C}_G = \alpha L_G$ satisfies

$$\mathfrak{C}_G \approx 4.86 - 3.48\varphi \tag{6}$$

to within 0.01 or better.

$\mathfrak{C}_G$ in Eq. (6) varies between 4.0 and 3.6 for $0.25 \le \varphi \le 0.35$. The values of $\mathfrak{C}_W = \alpha L_W$ for that model are expected smaller. This follows since it has been pointed out that L_G is biased towards the thickest regions in the microstructure [42]. By referring to the thinnest regions, L_W is systematically smaller.

How do experimental findings compare to the above considerations? Brunauer–Emmett–Teller (BET) adsorption studies by Detsi et al. [27] achieve good consistency by suggesting $\mathfrak{C} = 3.7$. It has been advertised that BET studies of NPG may contain artifacts, as the material tends to coarsen during the heating cycles that are required for removing physisorbed water, a prerequisite for meaningful BET data [26]. The adsorption would then not probe the original sample state, and the area value as well as $\mathfrak{C}$ might emerge erroneously low. Yet, the $\mathfrak{C}$ value of Detsi et al. is confirmed by the BET data of Tan et al. [28], which strengthens the result. It is noted that the sample size required for BET analysis ([26] recommends ~1 g of NPG, [27,28] each use ~250 mg, compared to ~8 mg/specimen in the present work) is not available in the routine studies of dealloyed nanoporous metal that are the target of our work.

Detsi et al. [27] also observed $\mathfrak{C} \approx 10$ based on electrochemical capacitance measurements. The authors argue in favor of their BET value, based on possible artifacts in their capacitance data. The other extreme

of values for $\mathfrak{C}$ comes from a study by Jeon et al. [34]. Analyzing the surface area in 3D tomographic reconstructions of NPG, that study finds $\mathfrak{C} = 1.0$. None of the two extremes is readily reconciled with the present understanding of the geometry of the NPG microstructure.

3. Materials and methods

3.1. Sample preparation

Ingots of the master alloy $Ag_{75}Au_{25}$ were prepared by arc melting the 99.995% pure constituents. The ingots were sealed in evacuated quartz tubes, homogenized at 1173 K for 120 h and wire-drawn to 1 mm diameter. Intermediate annealing at 1073 K for 600 s was carried out for recovery after every 20% reduction in diameter. A diamond wire saw served to section the wire into 2 mm long cylindrical master alloy samples. Finally, the master alloy was annealed at 1073 K for 2000 s in Ar.

A three electrode setup with a Ag/AgCl pseudo reference electrode (0.47 V vs. the standard hydrogen electrode, SHE) and a potentiostat (PGSTAT-302N) were used in all electrochemical processes. The pseudo reference electrode was calibrated with respect to SHE in the same electrolyte that was used for electrochemical processes. Potentials reported in this article are with respect to SHE.

Dealloying used a constant potential of 1.22 V in 1M $HClO_4$ (99.99%) and was stopped when the current decayed to 10 µA. The potential 1.32 V was then applied for 1200 s to further reduce the content in Ag. Next, we executed 20 potential cycles in the interval 0.07—1.57 V in a fresh 1M $HClO_4$. That latter procedure – hold and potential cycles – was repeated once, with the last cycle terminating at 0.77 V to achieve an adsorbate-free surface. Finally, the samples were rinsed in ultrapure water and dried in air.

Coarsening was induced by isothermal anneals in an infrared furnace (ULVAC MILA-5000) at a vacuum $<10^{-5}$ mbar. After the anneal, samples were again immersed in 1M $HClO_4$; they were first exposed to the potential 1.32 V for 1200 s and then to 20 potential cycles in the interval 0.07—1.57 V. This served to remove Ag, which accumulates on the ligament surfaces after coarsening [43,44]. The last cycle was terminated at 0.77 V to achieve an adsorbate-free surface.

The mass density was measured by recording sample dimensions with an optical measurement microscope, computing the volume and combining that information with the sample mass. The solid fraction was obtained by dividing through the mass density of the massive alloy, accounting for the (very small, see Results) residual Ag content.

3.2. Measuring the capacity

Our electrochemical characterization was based on the capacitance-ratio method in 1M $HClO_4$ (99.999%). That electrolyte is weakly adsorbing on gold; it is also commonly employed in the preparation of NPG and so is a natural choice for the characterization. Samples were cleaned and dried after preparation (dealloying and in some cases annealing) and were then exposed to fresh electrolyte for the characterization. The electrolyte was thoroughly purged with Ar (99.9999%) prior to the capacitive cycles.

The mean (over the absolute values in anodic and cathodic scans) current, I_c, relates to the net capacity, C, and to the electrode potential scan rate $\dot{E}$ according to $C = I_c/\dot{E}$. We inspected I_c in the center of a narrow potential window around $E = 0.82$ V. We applied scan rates spanning two orders of magnitude, plotted I_c versus $\dot{E}$, verified linear behavior and obtained C from the slope of the straight line (through the origin) of best fit according to $C = \mathrm{d}I_c/\mathrm{d}\dot{E}$.

As an intermediate step in the data reduction, we found it convenient to convert the experimental capacity data to volume-specific capacitance, c_v, according to

$$c_v = \frac{C}{V} = \frac{C\rho}{m}\,, \tag{7}$$

where V, ρ and m denote the net solid volume, the mass density of the solid phase and the sample mass, respectively. Our data analysis used the mass density of Au with residual Ag, here $\rho = 19.22\,\mathrm{g/cm^3}$.

The capacitance ratio method relates the surface area, A, to C and to the reference capacitance, c^*, of a planar Au surface under otherwise identical experimental conditions by $A = C/c^*$. This implies

$$\alpha = \frac{c_v}{c^*} \tag{8}$$

and, in view of Eq. (1),

$$L = c^*\mathfrak{C}\frac{1}{c_v} = \mathfrak{F}\frac{1}{c_v}\,. \tag{9}$$

Here, $\mathfrak{F} = \mathfrak{C}c^*$ is a conversion factor that relates the volume-specific capacitance of a porous specimen to its ligament size.

In principle, the α of our specimens could be determined using Eq. (8), and the value of the geometric constant $\mathfrak{C}$ would then follow from the L_W and Eq. (1). Yet, the high sensitivity of the reference capacitance values c^* to the electrode potential and surface crystallography (see Section 5.2) inflicts a substantial uncertainty in this approach. Here, we therefore use Eq. (9) to directly determine the conversion factor $\mathfrak{F}$. It is emphasized that this approach does not require knowledge of c^*. Thus, we establish a link between electron-micrograph-based and electrochemistry-based analysis of ligament size.

3.3. Electron microscopy

For investigation in the scanning electron microscope (SEM), specimens were fractured across the diameter after making a sharp notch with a scalpel. A Zeiss Supra 55VP FEG SEM, equipped with an Oxford X-Max 20 SDD Energy Dispersive X-ray (EDX) detector, was used to characterize the morphology and elemental composition on the fracture surfaces. Secondary electron images were taken at the accelerating voltage of 10 kV, using in-lens detector at a working distance of 3 mm. EDX microanalysis was performed at the accelerating voltage and working distance of 15 kV and 8 mm, respectively. The software ImageJ (v1.53k) [45] was used to measure line distances in the micrographs.

3.4. Generating numerical renderings of the leveled-wave model

Microstructures for studies of the leveled-wave model were based on algorithms described in [37], implemented in an algebra program (Wolfram Mathematica 11.3). A Gaussian random field in a simulation box of edge length b was generated by superimposing plane waves with wavevectors, $\mathbf{q}_i = 2\pi b^{-1}\{h_i, k_i, l_i\}$ with $\{h, k, l\}$ integers. The wavevectors were of identical magnitude, with $H = \sqrt{h_i^2 + k_i^2 + l_i^2} =$ const, and all compatible $\{h, k, l\}$ were used. The wavelength was $\lambda = 2\pi/|\mathbf{q}| = b/H$. Individual waves had random phase shifts. Two separate realizations of the model were generated with $H = \sqrt{146}$ (96 independent wavevectors) and $\sqrt{341}$ (168 wavevectors), respectively. For each realization, the Gaussian field was mapped onto the vertices of a simple cubic lattice (simulation box) of $100 \times 100 \times 100$ voxels.

Renderings of each structure were generated as contour graphs interpolating the random field at discrimination levels chosen for the desired solid volume fraction [37]. Their spatial scale was set by λ. The renderings were exported as 2D images and processed further by the identical image analysis procedures as the experiment. For each solid fraction, at least 5 renderings – each with a different set of random phase shifts – were examined, so that ~500 ligament diameters could be collected.

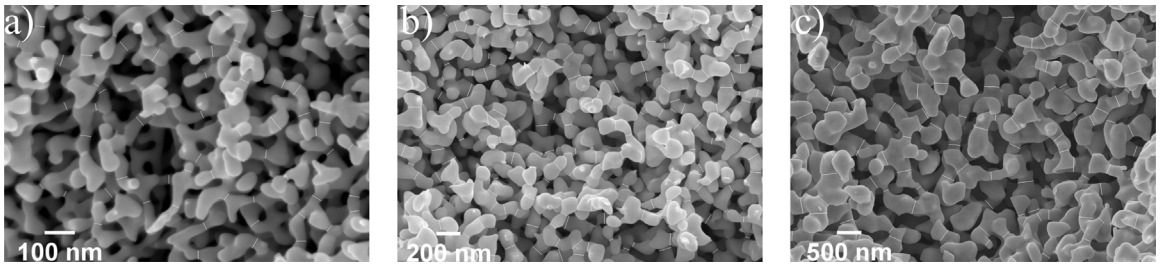

Fig. 1. Scanning electron micrographs of nanoporous gold at various states of annealing. (a) as dealloyed, (b) annealed at 573 K for 300 s and (c) annealed at 673 K for 2 h. Measured line distances marked in white.

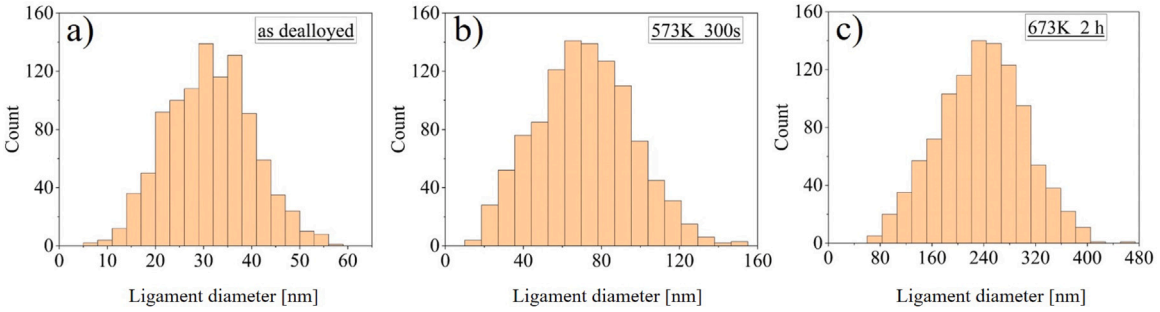

Fig. 2. Collections of measured ligament diameters are plotted in histograms with number of measurements as a function of ligament diameters for (a) as dealloyed and annealed specimens at (b) 573 K for 300 s and (c) at 673 K for 2 h.

Table 1
Solid fraction and its variation during annealing. For two exemplary samples, table shows ligament size, L, and solid fraction, φ, in as-dealloyed and annealed states.

	State	L [nm]	φ [no units]
Sample A	As dealloyed	41	0.27 ± 0.01
	Annealed 673 K 1 h	200	0.29 ± 0.01
Sample B	As dealloyed	35	0.26 ± 0.01
	Annealed 773 K 2 h	360	0.30 ± 0.01

4. Results

4.1. Residual ag fraction and solid fraction

We have investigated 17 samples in as-dealloyed or annealed states, with ligament sizes that turned out to cover the range ~20–400 nm. EDX analysis shows average residual silver contents 0.9 at%, and the as-dealloyed mass density was found in the interval $\varphi = 0.25 - 0.28$. Samples were found to densify slightly during annealing. Exemplary data is shown in Table 1. Our findings were compatible with solid fractions in the interval $\varphi = 0.28 \pm 0.03$ in all states, as prepared and annealed.

4.2. Mean ligament size from electron micrographs

The microstructure of cross-sectional fracture surfaces was taken as representative of the bulk of our samples. For each sample, we analyzed several scanning electron micrographs from one cross-section. In each micrograph, the diameter of the waist of each unambiguously identifiable ligament was measured, and the number of micrographs was chosen so that at least 1000 diameters were recorded for each specimen. Three exemplary micrographs, representative of different annealing conditions, are shown in Fig. 1; the examples cover the entire range of ligament sizes considered in this study. The white lines mark the diameters. The histograms in Fig. 2 represent the distribution of ligament sizes for the samples of Fig. 1. The bin sizes of the histograms were selected according to Scott's rule [46].

When sizes are normalized to their mean, the evolution – as the mean size increases – of the shape of the distribution provides an indication of the degree of microstructural self-similarity during coarsening. Here, we explore this issue. Rather than working with any specific model – such as the Weibull distribution [22] – for the size distribution, our analysis remains model-independent and, in that sense, uses unbiased statistical moments. Specifically, for each set comprising N ligament diameters L_j, we inspect the nth moments of the distribution,

$$\langle L \rangle_n = \frac{1}{N} \sum_j L_j^n , \tag{10}$$

or combinations thereof, and the standard deviation,

$$\sigma = \sqrt{\frac{1}{N} \sum \left(L_j - \langle L \rangle_1 \right)^2} . \tag{11}$$

Obviously, the conventional notion of mean SEM ligament size has $L_W = \langle L \rangle_1$.

Fig. 3 shows the standard deviations of our size distributions, plotted versus L_W; note the log–log scale. The data exhibits a quite precisely linear correlation, with $\sigma / L_W = 0.303 \pm 0.007$.

Importantly, we find the characteristics of the ligament size distributions quite precisely independent of the mean size, throughout the entire range of ligament sizes. This is at least consistent with the notion that the NPG morphologies remain self-similar during coarsening in that range of ligament sizes. Note that this range sensibly covers the ligament sizes of the majority of experimental studies in the field of NPG.

Besides the width σ of the size distribution, one may also ask for the confidence interval, $\pm \delta L_W$, for the mean L_W of the distribution. Specifically, we are interested in the uncertainty due to of the finite number of ligaments that were gauged. We base our estimate of δL_W on the bootstrap standard deviation [47]. From the data set with N_k sizes, many (here at least 1000) random samples of size N_k were collected, allowing for multiple occurrence of individual data. Each sample was analyzed for $\langle L \rangle_1$ and the standard deviation of the set of results identified with δL_W. We obtained $\delta L_W / L_W \approx 0.009$ for all samples, suggesting that the accuracy of our L_W is not limited by counting

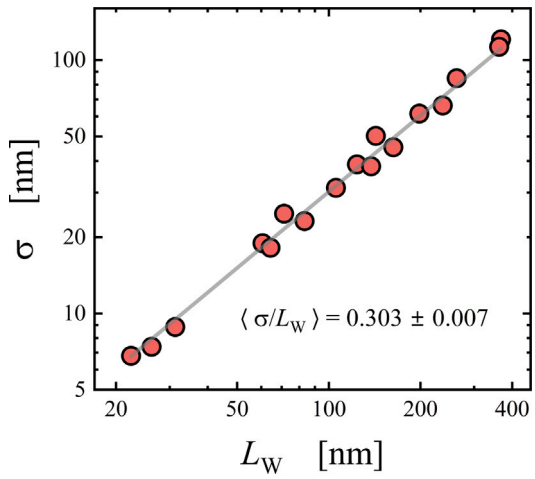

Fig. 3. Standard deviation, σ, of the ligament size distribution plotted versus the mean ligament size, L_W. Note logarithmic axis scales. Solid line: best fit with linear correlation; numerical correlation factor is indicated.

statistics. In fact, we found the bootstrap analysis to show a relative accuracy of 5% in $\delta L_W/L_W$ already with only 30 ligaments gauged. This suggests that the analysis of electron micrographs provides a quite efficient way of estimating the characteristic microstructural length scales of NPG, provided that the area analyzed is representative for the entire region of interest in the sample. That issue will be inspected next.

4.3. Heterogeneity on fracture surfaces

For any given NPG specimen, how homogeneous is the size distribution over the fracture surface? Our analysis contains information on that issue, since we explored several (typically 12–20) SEM frames distributed over the cross-section of any given sample. The data in Fig. 4 show the statistics explored separately for each individual frame, for five representative fracture surfaces (in other words, for five separate NPG specimens).

Each NPG specimen is represented, in Fig. 4a, by a group of data with an individual color. Each group displays a statistical analysis of several SEM frames. The circles are centered at the individual mean ligament sizes L_W^f of each frame, and the vertical lines represent the corresponding standard deviation σ^f. Horizontal error bars (located within the circles, as the uncertainty is very small) represent the bootstrap standard deviation δL_W^f.

For the samples of Fig. 4a, c compiles measures for the variability in size, in each case normalized to the respective L_W. Specifically, orange bars in the figure represent the average, over all frames of a cross-sectional surface, of the standard deviations in the individual frames. Conversely, green bars represent the standard deviation of the frame-wise mean size values. The former value may be considered as representing the inherent size-distribution width of NPG. It is seen to substantially exceed the variation in the mean size values between the different frames. That implies that the dominant contribution to the size distribution width is inherent, and that heterogeneity across the fracture surface is comparatively minor.

The yellow bars in Fig. 4c represent the bootstrap standard deviations from entire fracture surfaces (all frames). These are small, indicating that the mean size is measured precisely. Yet, the distribution width (as just discussed) is much larger.

The violet bars in Fig. 4c represent the mean bootstrap standard deviations from individual frames. These are larger than the all-frame ones, simply because of the lesser counting statistics. Yet, they are typically smaller than the frame-by-frame variation in mean size, indicating that the above-mentioned finding on a small but noticeable heterogeneity across the fracture surface is real, not an artifact of counting statistics.

While the just-mentioned statements appear sensibly valid for all specimens, one may note that those specimens which were subjected to annealing exhibit slightly more macroscopic heterogeneity.

4.4. Characterizing size by cyclic voltammetry

Fig. 5(a) presents overview of cyclic voltammograms (CVs) for specimens with different L_W. The graphs show the total current in each sample, for samples with comparable total mass. The current magnitude decreases as L_W increases, in agreement with the expected decrease in surface area. Oxidation/reduction reactions take place at potentials >0.9 V, while capacitive charging dominates at $E < 0.9$ V. For our capacitance measurements, we selected the region of least capacitance and least Faraday current, namely the potential window 0.82 ± 0.05 V indicated by the gray box in Fig. 5(b).

Fig. 6(a) shows capacitive CVs for an $L_W = 71$ nm specimen at different $\dot{E}$. It can be seen that the voltammograms and all scan rates are featureless, as expected for capacitive processes. The square aspect at the lowest scan rates suggests negligible transport limitations there. Furthermore, the symmetry of those CVs suggests small (note the logarithmic current axis and the extremely small net current magnitude there) Faraday current contributions. In our analysis of the capacitive current, these were compensated by averaging over anodic and catholic scan directions.

Fig. 6b exemplifies our graphs of the currents I_c (see Section 3.3) versus $\dot{E}$, here for the specimen of Fig. 6a. A linear fit through the origin is in excellent agreement with the data, which spans more than one order of magnitude in $\dot{E}$. Linear regression provides the slope of the fit line, which in turn implies the net capacities C, as outlined in Section 3.3.

Fig. 7(a) shows how the volume-specific capacitance, c_v, varies as the function of L_W. In log–log representation, the data agree well with a straight line of slope −1, as is expected if the net capacity scales with the area of surface, which in turn scales inversely with the ligament size. The bold line in the figure is a straight line of best fit, constrained to slope −1, confirming the just mentioned observation.

We have determined $\mathfrak{F}$ from the straight line of best fit to the data of Fig. 7(a) with number average ligament sizes L_W in the abscissa. The bold line in the figure is a straight line of best fit with slope −1; its Pearson correlation coefficient of −0.97 confirms the inverse correlation between capacitance and the measures for ligament size from SEM. In Fig. 7, the propagated error from c_V is not larger than the size of the circles representing the experimental data points. Obviously, the scatter around the fit line considerably exceeds that standard deviation (see Section 5.4). We hypothesize that the scatter is due to heterogeneity, over the sample volume, in ligament size. This implies that the confidence limits for our fit parameters are set by the standard deviation of their residuals. In that sense, the constant of proportionality for conversion between the two approaches to ligament size is $\mathfrak{F} = 192 \pm 10\,\mu F/cm^2$, when number average ligament size L_W is the parameter of interest. The shaded region in the graph represents that confidence interval.

4.5. Relations between measures of ligament size

Our value of $\mathfrak{F}$ is indirectly based on the volume-specific surface areas α from the volume-specific capacitance data of Fig. 7.

Note that the histograms of Fig. 2 illustrate that the ligament size distribution has a finite width. The net values of volume, V, and of area, A, in a nanoporous sample may then be expressed as weighted averages over the ligament size distribution. Assuming ligaments of different L to be geometrically similar, one has

$$\alpha = \frac{A}{V} \propto \frac{\sum L_j^2}{\sum L_j^3} = \frac{\langle L \rangle_2}{\langle L \rangle_3}, \tag{12}$$

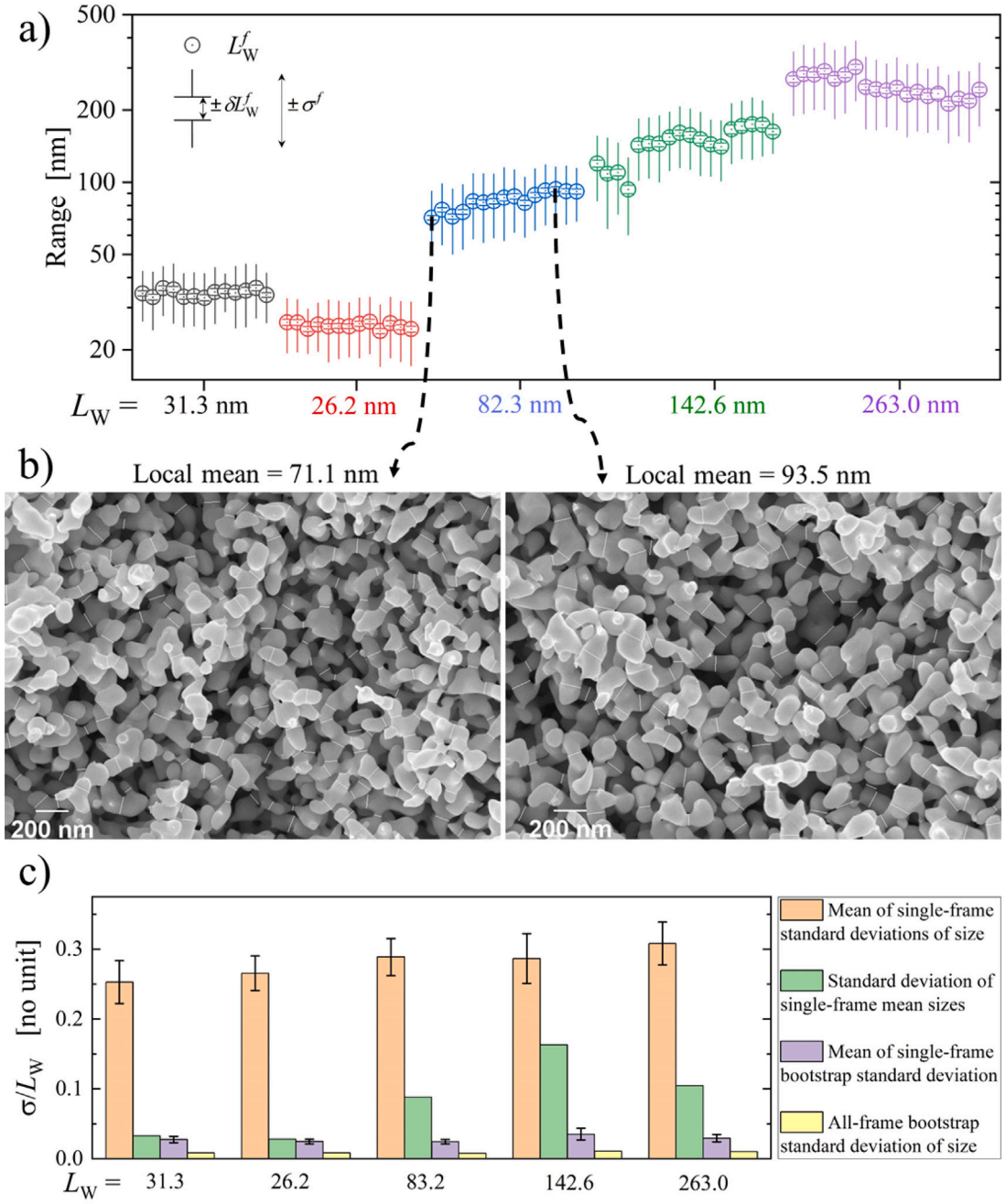

Fig. 4. Distribution of sizes on cross-sectional fracture surfaces of representative samples, resolved by individual frame or compiled for all frames on the cross-section. (a) Frame-wise data, grouped by sample (colors). Circles: mean ligament size, L_W^f: vertical lines, ligament size standard deviation σ^f; error bars (inside circles): bootstrap errors δL_W^f. (b) Example for electron micrographs, here for two different locations on same fracture surface, selected for maximum difference in local mean ligament size (dashed lines connecting to panel (a)). Specimen annealed at 573 K for 120 s with $L_W = 82.3$ nm. (c) Data for samples of panel (a). Color-coded histogram bars represent: orange: mean of the standard deviations in the individual frames; green: standard deviation of the frame-wise mean size values; violet: mean of bootstrap standard deviations for individual frames, and yellow: bootstrap standard deviations from entire fracture surface (all frames). All data is normalized to respective L_W. (For interpretation of the references to color in this figure legend, the reader is referred to the web version of this article.)

where the summations are over all ligaments, as in Eq. (10). Eq. (12) suggests an area-weighted mean ligament waist diameter, $\langle L \rangle_A$, defined as

$$\langle L \rangle_A = \frac{\sum A_j L_j}{\sum A_j} = \frac{\langle L \rangle_3}{\langle L \rangle_2}, \tag{13}$$

as a natural variable determining the area of surface. Averaging over all experimental data of our study, we find $\langle L \rangle_A / L_W = 1.17$. For a Gaussian size distribution with the standard deviation of our Fig. 3, the analytical value would be 1.165, practically identical.

In the spirit of Eqs. (12) and (13), $\langle L \rangle_A$ is expected to relate to α and to the capacitance by

$$\langle L \rangle_A = \frac{\mathfrak{C}_A}{\alpha} = \frac{\mathfrak{F}_A}{c_V}, \tag{14}$$

where $\mathfrak{C}_A$ and $\mathfrak{F}_A$ represent scaling factors for use with the area-weighted average ligament size.

We have determined $\mathfrak{F}_A$ as the straight line of best fit to the plot of capacitance versus $\langle L \rangle_A$ in Fig. 7(b). It is re-emphasized that the area-weighted size must be preferred when one aims at a meaningful comparison with L_α. The correlation factor emerges here as $\mathfrak{F}_A$ =

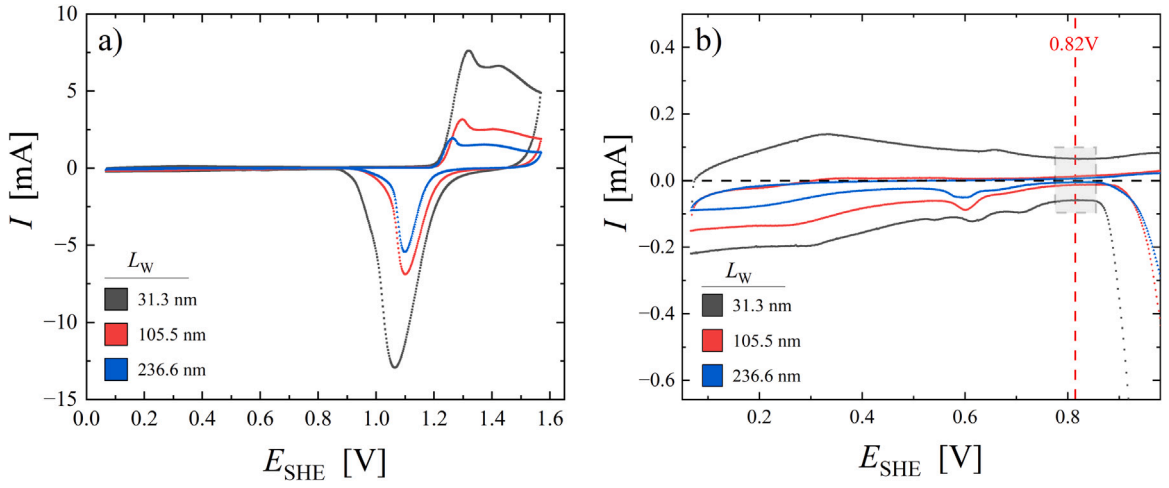

Fig. 5. Overview of cyclic voltammograms in 1M $HClO_4$ for samples with different ligament size. Full range of potential is shown in (a); current variation at the more cathodic potentials is shown enlarged in (b). Gray box denotes capacitive region around 0.82 V that was used for capacitance ratio measurements. Scan rate $\dot{E} = 10\,\mathrm{mV\,s^{-1}}$. (For interpretation of the references to color in this figure legend, the reader is referred to the web version of this article.)

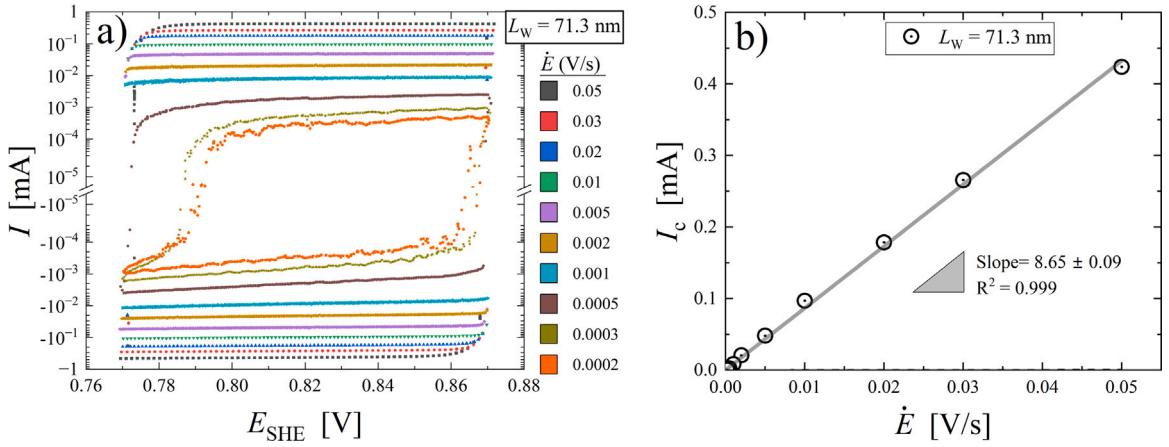

Fig. 6. (a) Example for evolution of cyclic voltammograms with potential scan rate, $\dot{E}$, in the potential regime selected for capacitance ratio measurements. Net electrode current I versus electrode potential E for a nanoporous gold sample annealed at 573 K for 300 s, with ligament size 71.3 nm. Color codes for $\dot{E}$ are indicated by legend. (b) The average of absolute currents I_c is plotted as a function of scan rates ($\dot{E}$) for the same specimen. Corresponding slope of the linear fits with zero intercept is indicated in the figure.

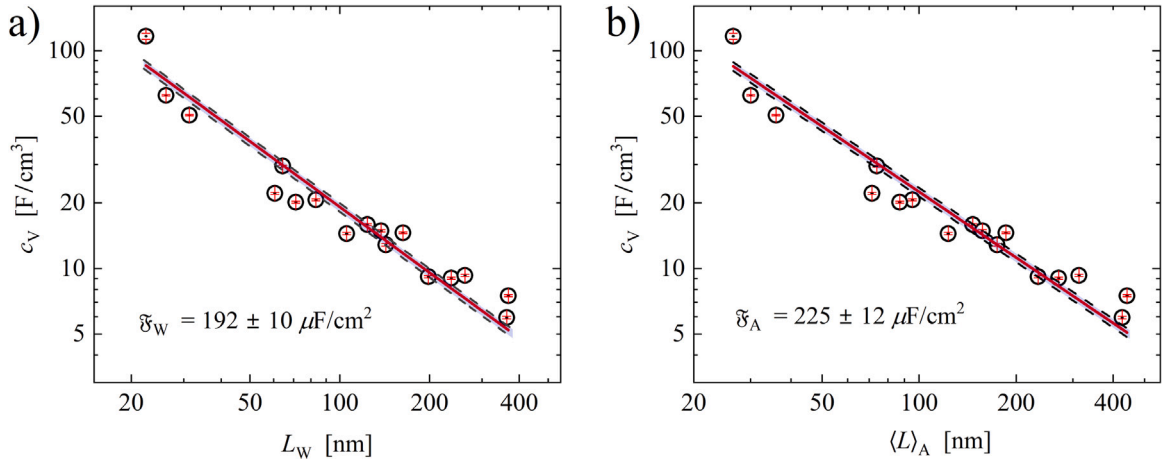

Fig. 7. Variation of the experimental volume-specific capacitance, c_v, with the electron-microscopy derived mean ligament size, L_W (a) and area-weighted ligament size, $\langle L\rangle_A$ (b). Symbols: data; line: straight line of best fit, illustrating linear correlation.

$225 \pm 12\,\mu F/cm^2$. This is higher than $\Im_W$ in panel (a) of Fig. 7. Quite generally, $\langle L\rangle_A > L_W$, which can be understood as an example for Chebyshev's inequality [48], $\langle L\rangle_3 \geq \langle L\rangle_2\langle L\rangle_1$, and as a consequence of larger ligaments receiving more weight in the area-weighted averaging.

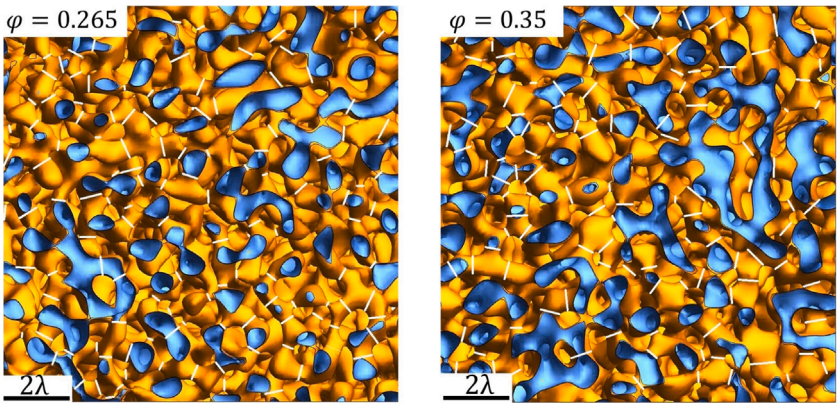

Fig. 8. Renderings of leveled-wave structures. Examples for solid fractions φ = 0.265 and 0.35. Golden contour: outer surface of solid phase; blue: inner space of solid phase. Measured line distances marked in white. Scale bars are indicated in units of the wavelength λ. (For interpretation of the references to color in this figure legend, the reader is referred to the web version of this article.)

4.6. Ligament diameters of leveled-wave structures

As the leveled-wave model provides links between various metrics for size, it is of interest to connect our $L_W - \alpha$ relation to that model. We have numerically determined L_W of leveled-wave renderings – such as the examples in Fig. 8 – for four solid fractions in the range 0.25—0.35, applying the identical image evaluation procedures as for the experiment.

The ratio of mean distances between the ligament centers $\tilde{L}$, Eq. (4), to L_W is plotted in Fig. 9a as a function of solid fraction. The ratio decreases with increasing solid fraction; this reflects the thickening of the ligaments and the narrowing of the intervening pore channels at higher φ.

As an analogy to the analysis of experimental data in Fig. 3, Fig. 9b shows the model's σ/L_W as a function of solid fraction. Within the confidence limits of our evaluation, the scaled distribution width appears independent of the solid fraction. Furthermore, at $\sigma/L_W = 0.30$, the normalized width actually agrees precisely with the experiment. This provides one more instance where the leveled-wave model closely emulates experimental NPG.

Lastly, our numerical analysis supplies a value for the scaling factor $\mathfrak{C}_W = \alpha L_W$ for leveled-wave structures. This is obtained by combining the numerical L_W with α as obtained from Eq. (3). In view of the discussion in Section 4.5, we evaluate both scaling factors, $\mathfrak{C}_W = \alpha L_W$ for use with the mean ligament size and $\mathfrak{C}_A = \alpha \langle L \rangle_A$ for use with the area-weighted average size. Fig. 9c shows that these quantities emerge as $\mathfrak{C}_W = 3.03 \pm 0.02$ and $\mathfrak{C}_A = 3.53 \pm 0.03$; these coefficients are again independent of φ within the confidence limits of our data.

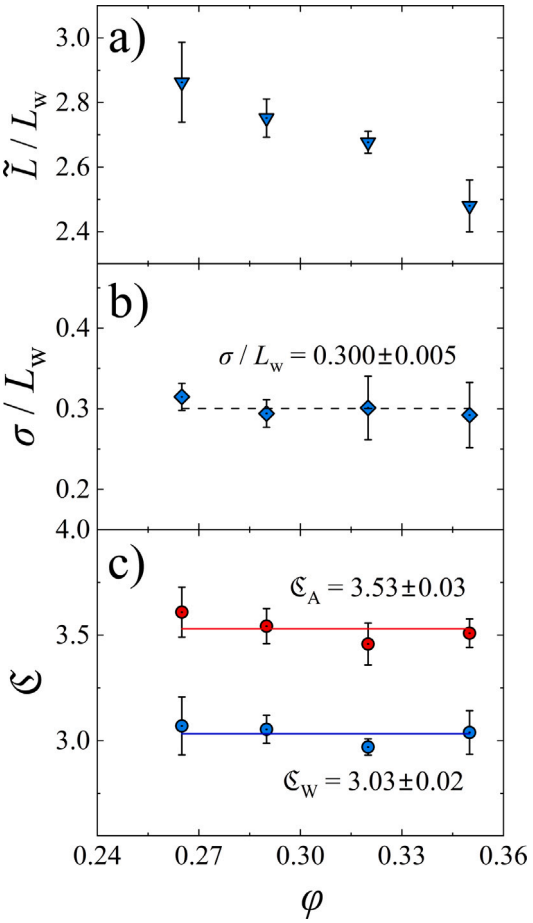

Fig. 9. Evaluation of leveled-wave ligament sizes for renderings with different solid fraction φ. (a), ratio of characteristic spacing between neighboring ligaments centers, $\tilde{L}$, over mean ligament diameter L_W. (b), ligament-size distribution width σ scaled to L_W. Dashed horizontal line: mean value. (c), number- and area-weighted scaling factors, $\mathfrak{C}_W$ (blue) and $\mathfrak{C}_A$ (red), respectively. Horizontal lines: mean values. Ligament size, distribution width and scaling factor were independently determined for each of at least five renderings at the solid fraction in question; data points show mean (symbols) and standard deviation (error bars). (For interpretation of the references to color in this figure legend, the reader is referred to the web version of this article.)

5. Discussion

5.1. Ligament sizes from electron microscopy and from electrochemistry

One aim of our study was identifying a conversion rule that affords measuring the ligament size of NPG based on an electrochemical-capacitance-ratio based approach. We found a highly significant correlation between volume-specific capacitance and ligament size, supporting that both approaches consistently characterize the same microstructural feature. Reduction of the experimental data can produce values of the SEM ligament sizes L_W and $\langle L \rangle_A$ as well as the volume-specific capacitance c_v, and this does not require choosing a reference capacitance value. Our analysis applies to experiments that use the same electrolyte and potential as in the present study.

5.2. Ligament size distribution

Analyzing dimension of microstructural features from micrographs, such as L_W in our study, is ubiquitous in materials science as a method for characterizing the size distribution. For NPG, L_W at the external surface has been found smaller compared to the bulk [23,25]. This suggests measuring L_W on fracture surfaces that represent the bulk microstructure, especially if one aims at a comparison with L_α from electrochemical characterization, which probes the entire sample volume.

The standard deviation of the ligament size scales with the size according to $\sigma/L_W = 0.303 \pm 0.007$. This suggests somewhat more narrow distributions than those of Badwe et al. [22]. Those authors report $\sigma/L = 0.35$, based on skeletonization of 2D micrographs combined with a Euclidean distance transform. That approach averages over the entire microstructure, including the thicker regions in the nodes where ligaments meet. Our approach of measuring L_W at the waists of ligaments systematically discards the nodes, and this may explain the narrower distribution in our study. With that in mind, we tend to qualify the two studies as well consistent.

Significantly, the leveled-wave model has $\sigma/L_W = 0.300 \pm 0.005$, in precise agreement with the experiment. Since the model is free of heterogeneity by construction, the agreement supports the notion of the size distribution width as inherent.

5.3. Microstructural heterogeneity

The SEM data may be discussed with regard to two types of heterogeneity. Firstly, the variance of the ligament size within the smallest regions of interest, namely single SEM micrographs, relates to the inherent size distribution of the NPG microstructure, with a standard deviation of $0.303 L_W$. Secondly, there is a small but noticeable macroscopic heterogeneity along the sample cross-section, as it is exposed along a fracture surface. This effect is enhanced in the coarsened specimens, suggesting a relation to the processing procedures. Yet, we found that the inherent distribution width is considerably higher than the variation in L due to the heterogeneity.

The constant relative width of the size distribution would seem to suggest self-similar coarsening. Yet, studies of the mechanical behavior of coarsened NPG have established important deviations from self similar coarsening [49], in the form a gradual loss in network connectivity. Direct analysis of the connectivity in numerical simulation of coarsening supports the finding, specifically for NPG with solid fraction $\varphi < 0.30$ [50]. At initial values of $\varphi = 0.26 - 0.27$, our samples are just within the non-self-similar range. We speculate that the loss in connectivity, which strongly affects the mechanics, leaves an at best weak signature in the ligament size distribution.

5.4. Scaling factors $\mathfrak{C}$ – values and a sensible upper limit

For the scaling factors $\mathfrak{C}$ of leveled-wave structures, we report $\mathfrak{C}_W = 3.03$ and $\mathfrak{C}_A = 3.53$. Those values are smaller than the $\mathfrak{C} = 3.7$ suggested for experimental NPG [27]. We take this as an incentive to inspect the range of permissible values for the $\mathfrak{C}$.

As outlined in Section 2, idealized networks made of monodisperse cylindrical ligaments of diameter L have $\mathfrak{C} = 4$. For experiments with more realistic ligament shapes of nonuniform diameter, and measuring L at the thinnest cross-section, $\mathfrak{C} = 4$ is an upper limit: as all remaining regions then have larger diameter than L, their individual areas per volume are less and so the net αL for each ligament segment is less than 4. A more formal analysis in the Supporting Information (SI) confirms this statement. The expected value of α is further reduced since the nodes where ligaments meet also contribute an increased local diameter and a locally reduced area per volume.

The nodes and the convexity of the ligaments are not the only microstructural features imposing an upper bound. Consider a network of cylindrical ligaments with a Gaussian size distribution of median L_0 and standard deviation σ. The moments of Section 4.2 are then well approximated[1] by

$$\langle L\rangle_1 = L_0\,, \tag{15}$$

$$\langle L\rangle_2 = L_0^2\left(1+(\sigma/L_0)^2\right)\,, \tag{16}$$

$$\langle L\rangle_3 = L_0^3\left(1+3(\sigma/L_0)^2\right)\,. \tag{17}$$

With $L_W = \langle L\rangle_1$, with $\langle L\rangle_A = \langle L\rangle_3/\langle L\rangle_2$, with 4 the upper limit for αL of each ligament (see above), and with $\alpha \propto \langle L\rangle_2/\langle L\rangle_3$ for the distribution one immediately finds

$$\mathfrak{C}_A := \alpha\langle L\rangle_A < 4\frac{\langle L\rangle_2}{\langle L\rangle_3}\frac{\langle L\rangle_3}{\langle L\rangle_2} = 4\,, \tag{18}$$

$$\mathfrak{C}_W := \alpha L_W < 4\frac{\langle L\rangle_2}{\langle L\rangle_3}\langle L\rangle_1 = 4\frac{1+(\sigma/L_0)^2}{1+3(\sigma/L_0)^2}\,. \tag{19}$$

The σ-dependent term in Eq. (19) is always <1. This reflects that $\langle L\rangle_1 < \langle L\rangle_A$, since number-weighted averaging gives less weight to the larger sizes in the distribution. Specifically for the present structures with $\sigma/L_W = 0.300 \pm 0.005$, Eq. (19) implies

$$\mathfrak{C}_W < 3.43 \pm 0.03\,. \tag{20}$$

Within its narrow error margin, the upper bound value for $\mathfrak{C}_W$ of Eq. (20) is confirmed when the number- and area-weighted average sizes are computed from our empirical size histograms rather than the Gaussian distribution.

To summarize, the convexity of ligaments in NPG together with the definition of L_W in terms of diameters at the narrowest section imply $\mathfrak{C} < 4$ for each individual ligaments, and the width of the size distribution along with the scaling of α with an area-weighted average imply that the number-weighted $\mathfrak{C}$ must again be smaller. Eq. (20) presents the ensuing upper bound when the normalized size distribution width σ/L_W is that of NPG or of the leveled-wave model.

In their analysis of the ligament shape in the 3D tomographic reconstructions of experimental NPG by Hu et al. [33], Richert and Huber [51] have explicitly confirmed that the overwhelming majority of ligaments is convex in the sense of a single thinnest cross-section near the center of the ligament. Thus, area per volume of individual ligaments may be expected quite noticeably <4, and the actual value of $\mathfrak{C}_W$ may be expected noticeably below the upper bound Eq. (20).

We note that our numerical values of $\mathfrak{C}_W$ and $\mathfrak{C}_A$ for leveled-wave structures are consistent with the above bounds. By contrast, as $\mathfrak{C}$ in [27] is based on a number-weighted mean ligament size, its value 3.7 conflicts with Eq. (20). This suggests that the $\mathfrak{C}_W$ value of NPG may be closer to that of the leveled-wave model than what is suggested by the data in [27].

Since α is uniquely defined, the $\mathfrak{C}$ for various size metrics of one and the same structure scale with the value of the metric. Thus, comparing the $\mathfrak{C}$ provides the corresponding conversion factors. Table S1 in the SI compiles the $\mathfrak{C}$ of the leveled wave model.

How is the comparison between SEM- and capacitance-based data in the present work compatible with leveled-wave data for $\mathfrak{C}$? Our leveled-wave value is $\mathfrak{C}_A = 3.53 \pm 0.03$. In conjunction with $c^* = \mathfrak{F}_A/\mathfrak{C}_A$ (see Eq. (9)), this implies $c^* = 63.7 \pm 2.3\,\mu F/cm^2$. Measurements on single-crystalline gold electrodes at our value of E_{SHE} exhibit smaller c^*, in the range $25 - 45\,\mu F\,cm^{-2}$ [52,53]. Yet, data for polycrystalline Au in $0.5M\,HClO_4$ at $E_{SHE} = 0.82\,V$ [54] put the capacitance at $c^* = 64\,\mu F\,cm^{-2}$, which agrees amazingly well with our observation for leveled-wave data. In other words, even though the reference capacitance values per se are not known with sufficient confidence

[1] The approximation resides in replacing the physical lower bound $L = 0$ by the analytically more convenient $L = -\infty$ in integrals over the weighted normal distribution. For σ in the order of the present value 0.3, the ensuing relative error in the moments is $\ll 10^{-4}$.

and precision to afford an independent determination of the dimensionless scaling parameters $\mathfrak{C}$ in our experiment, our observations are not inconsistent with agreement between the scaling parameters of the leveled-wave model and experimental NPG.

6. Conclusions

Working with a set of samples spanning the ligament size range from 20 to 400 nm, our study explores measures for the ligament size in nanoporous gold (NPG).

Even though our investigation of the ligament size distribution by scanning electron microscopy is based on at least 1000 size readings for each sample, we find that – for the present, narrow distribution – counting as few as 30 ligaments affords estimating the mean size to within 5%. Heterogeneity over the cross-section of our millimeter-sized samples is detectable, yet the major part of the size distribution width is expressed at any location and so appears to be intrinsic to the NPG microstructure. Indeed, the practically identical value is found in the leveled-wave model, which is free of mesoscale heterogeneity by construction.

We find that a normalized standard deviation of the size remains invariant during coarsening, and that the net volume-specific double layer capacitance (per volume of the solid phase) is inversely proportional to the ligament size as determined from scanning electron micrographs. Both observations are consistent with a self-similar geometry, independent of the ligament size. This, together with the numerical agreement in the size distribution widths, qualifies experimental NPG and the leveled-wave model as closely matched microstructures.

Studies of the mechanical behavior of NPG have established that the connectivity within the network of ligaments may drastically change during coarsening, and this is confirmed by numerical simulation of coarsening. Clearly, therefore, not all aspects of the microstructural evolution of NPG are consistent with self similarity. Yet, those deviations appear not to significantly affect the ligament size distribution.

It is challenging to accurately determine absolute values of the specific surface area by electrochemical approaches, since reference capacitance values must be expected to depend sensibly on the experimental conditions. Our protocol for converting experimental volume-specific capacitance data of NPG into equivalent ligament size values avoids this problem, as it is calibrated against SEM data rather than capacitance data for planar gold surfaces. Size and inverse specific surface area of NPG are found linearly correlated over the entire range of sizes investigated, with a narrow confidence limit. This qualifies the present protocol as robust for characterizing nanoporous metals.

The product, $\mathfrak{C}$, of size and specific surface area is a dimensionless parameter characteristic of a microstructural morphology. For leveled wave structures, we find the numerical value $\mathfrak{C}_A \approx 3.5$, consistent with our discussion of upper bounds. The remarkable similarities of the NPG structures to the model suggest that this value may also be expected for NPG. This is not inconsistent with the electrochemical characterization and with reported capacitance data for polycrystalline Au under similar experimental conditions.

These observations add support to our protocol, suggesting nondestructive electrochemical characterization as a practicable alternative to the destructive investigation of the bulk ligament size of NPG by scanning electron microscopy. They also lend further support to the combination of NPG and the leveled-wave model as a showcase for investigating the microstructure of random network materials.

Declaration of competing interest

The authors declare that they have no known competing financial interests or personal relationships that could have appeared to influence the work reported in this paper.

Acknowledgment

This work was supported by the German Research Foundation (DFG) through grant WE1424/17-2, project 269855351, within the Research Unit FOR2213 “Nanoporous Gold – a Prototype for a Rational Catalyst Design”.

Appendix A. Supplementary data

Supplementary material related to this article can be found online at https://doi.org/10.1016/j.actamat.2023.119333.

References

[1] R. Li, K. Sieradzki, Ductile-brittle transition in random porous Au, Phys. Rev. Lett. 68 (8) (1992) 1168–1171.
[2] J. Erlebacher, M.J. Aziz, A. Karma, N. Dimitrov, K. Sieradzki, Evolution of nanoporosity in dealloying, Nature 410 (6827) (2001) 450–453.
[3] J. Snyder, I. McCue, K. Livi, J. Erlebacher, Structure/processing/properties relationships in nanoporous nanoparticles as applied to catalysis of the cathodic oxygen reduction reaction, J. Am. Chem. Soc. 134 (20) (2012) 8633–8645.
[4] N. Mameka, K. Wang, J. Markmann, E.T. Lilleodden, J. Weissmüller, Nanoporous gold—Testing macro-scale samples to probe small-scale mechanical behavior, Mater. Res. Lett. 4 (1) (2016) 27–36.
[5] J. Weissmüller, K. Sieradzki, Dealloyed nanoporous materials with interface-controlled behavior, Mrs Bull. 43 (1) (2018) 14–19.
[6] G. Wittstock, M. Bäumer, W. Dononelli, T. Küner, L. Lührs, C. Mahr, L.V. Moskaleva, M. Oezaslan, T. Risse, A. Rosenauer, et al., Nanoporous gold: From structure evolution to functional properties in catalysis and electrochemistry, Chem. Rev. 123 (10) (2023) 6716–6792.
[7] K. Michelsen, H. De Raedt, J.T.M. De Hosson, Aspects of mathematical morphology, Adv. Imaging Electron. Phys. 125 (2003) 119–194.
[8] E.T. Lilleodden, P.W. Voorhees, On the topological, morphological, and microstructural characterization of nanoporous metals, MRS Bull. 43 (1) (2018) 20–26.
[9] M. Ziehmer, E.T. Lilleodden, The isothermal evolution of nanoporous gold from the ring perspective-an application of graph theory, Acta Mater. 199 (2020) 669–679.
[10] S. Kucheyev, J. Hayes, J. Biener, T. Huser, C. Talley, A. Hamza, Surface-enhanced Raman scattering on nanoporous Au, Appl. Phys. Lett. 89 (5) (2006) 053102.
[11] L.H. Qian, A. Inoue, M.W. Chen, Large surface enhanced Raman scattering enhancements from fracture surfaces of nanoporous gold, Appl. Phys. Lett. 92 (9) (2008).
[12] J. Zhang, P. Liu, H. Ma, Y. Ding, Nanostructured porous gold for methanol electro-oxidation, J. Phys. Chem. C 111 (28) (2007) 10382–10388.
[13] A. Wittstock, A. Wichmann, J. Biener, M. Baumer, Nanoporous gold: a new gold catalyst with tunable properties, Faraday Discuss. 152 (2011) 87–98.
[14] L.H. Shao, H.J. Jin, J. Weissmüller, Actuation with high-surface-area materials, in: Nanoporous Gold: From an Ancient Technology To a High-Tech Material; RSC Nanoscience & Nanotechnology, Vol. 22, in: RSC Nanoscience and Nanotechnology, Royal Society of Chemistry, Cambridge, UK, 2012, pp. 137–166, Shao, L.-H. Jin, H.-J. Weissmueller, J..
[15] J. Biener, A.M. Hodge, J.R. Hayes, C.A. Volkert, L.A. Zepeda-Ruiz, A.V. Hamza, F.F. Abraham, Size effects on the mechanical behavior of nanoporous Au, Nano Lett. 6 (10) (2006) 2379–2382.
[16] C.A. Volkert, E.T. Lilleodden, D. Kramer, J. Weissmüller, Approaching the theoretical strength in nanoporous Au, Appl. Phys. Lett. 89 (6) (2006) 061920.
[17] N.J. Briot, T.J. Balk, Developing scaling relations for the yield strength of nanoporous gold, Phil. Mag. 95 (27) (2015) 2955–2973.
[18] H.-J. Jin, J. Weissmüller, D. Farkas, Mechanical response of nanoporous metals: A story of size, surface stress, and severed struts, MRS Bull. 43 (1) (2018) 35–42.
[19] M.M. Biener, J. Biener, A. Wichmann, A. Wittstock, T.F. Baumann, M. Baeumer, A.V. Hamza, ALD functionalized nanoporous gold: Thermal stability, mechanical properties, and catalytic activity, Nano Lett. 11 (8) (2011) 3085–3090.
[20] I. McCue, E. Benn, B. Gaskey, J. Erlebacher, Dealloying and dealloyed materials, Annu. Rev. Mater. Res. 46 (1) (2016) 263–286.
[21] E.-J. Gwak, J.-Y. Kim, Weakened flexural strength of nanocrystalline nanoporous gold by grain refinement, Nano Lett. 16 (4) (2016) 2497–2502.
[22] N. Badwe, X. Chen, K. Sieradzki, Mechanical properties of nanoporous gold in tension, Acta Mater. 129 (2017) 251–258.
[23] M. Graf, B. Roschning, J. Weissmüller, Nanoporous gold by alloy corrosion: Method-structure-property relationships, J. Electrochem. Soc. 164 (4) (2017) C194.
[24] B. Zandersons, L. Lührs, Y. Li, J. Weissmüller, On factors defining the mechanical behavior of nanoporous gold, Acta Mater. 215 (2021) 116979.
[25] S. Cattarin, D. Kramer, A. Lui, M.M. Musiani, Preparation and characterization of gold nanostructures of controlled dimension by electrochemical techniques, J. Phys. Chem. C 111 (34) (2007) 12643–12649.

[26] Y. Liu, S. Bliznakov, N. Dimitrov, Comprehensive study of the application of a pb underpotential deposition-assisted method for surface area measurement of metallic nanoporous materials, J. Phys. Chem. C 113 (28) (2009) 12362–12372.
[27] E. Detsi, E. De Jong, A. Zinchenko, Z. Vuković, I. Vuković, S. Punzhin, K. Loos, G. ten Brinke, H.A. De Raedt, P.R. Onck, J.T.M. De Hosson, On the specific surface area of nanoporous materials, Acta Mater. 59 (20) (2011) 7488–7497.
[28] Y.H. Tan, J.A. Davis, K. Fujikawa, N.V. Ganesh, A.V. Demchenko, K.J. Stine, Surface area and pore size characteristics of nanoporous gold subjected to thermal, mechanical, or surface modification studied using gas adsorption isotherms, cyclic voltammetry, thermogravimetric analysis, and scanning electron microscopy, J. Mater. Chem. 22 (14) (2012) 6733–6745.
[29] E. Rouya, S. Cattarin, M. Reed, R. Kelly, G. Zangari, Electrochemical characterization of the surface area of nanoporous gold films, J. Electrochem. Soc. 159 (4) (2012) K97.
[30] C. Lakshmanan, R.N. Viswanath, S.R. Polaki, R. Rajaraman, S. Dash, A.K. Tyagi, Surface area of nanoporous gold: Effect on temperature, Electrochim. Acta 182 (2015) 565–572.
[31] Y.-c.K. Chen-Wiegart, S. Wang, Y.S. Chu, W. Liu, I. McNulty, P.W. Voorhees, D.C. Dunand, Structural evolution of nanoporous gold during thermal coarsening, Acta Mater. 60 (12) (2012) 4972–4981.
[32] K.R. Mangipudi, E. Epler, C.A. Volkert, Morphological similarity and structure-dependent scaling laws of nanoporous gold from different synthesis methods, Acta Mater. 140 (2017) 337–343.
[33] K. Hu, M. Ziehmer, K. Wang, E.T. Lilleodden, Nanoporous gold: 3D structural analyses of representative volumes and their implications on scaling relations of mechanical behaviour, Phil. Mag. (2016) 1–14.
[34] H. Jeon, N.-R. Kang, E.-J. Gwak, J.-i. Jang, H.N. Han, J.Y. Hwang, S. Lee, J.-Y. Kim, Self-similarity in the structure of coarsened nanoporous gold, Scr. Mater. 137 (2017) 46–49.
[35] S. Trasatti, O. Petrii, Real surface area measurements in electrochemistry, J. Electroanal. Soc. 327 (1–2) (1992) 353–376.
[36] J.W. Cahn, Phase separation by spinodal decomposition in isotropic systems, J. Chem. Phys. 42 (1) (1965) 93–99.
[37] C. Soyarslan, S. Bargmann, M. Pradas, J. Weissmüller, 3D stochastic bicontinuous microstructures: Generation, topology and elasticity, Acta Mater. 149 (2018) 326–340.
[38] S. Shi, Y. Li, B.-N. Ngo-Dinh, J. Markmann, J. Weissmüller, Scaling behavior of stiffness and strength of hierarchical network nanomaterials, Science 371 (6533) (2021) 1026–1033.
[39] C.J. Gommes, Stochastic models of disordered mesoporous materials for small-angle scattering analysis and more, Microporous Mesop. Mater. 257 (2018) 62–78.
[40] H.J. Jin, S. Parida, D. Kramer, J. Weissmüller, Sign-inverted surface stress-charge response in nanoporous gold, Surf. Sci. 602 (23) (2008) 3588–3594.
[41] T. Hildebrand, P. Rüegsegger, A new method for the model-independent assessment of thickness in three-dimensional images, J. Microsc. 185 (1) (1997) 67–75.
[42] C. Richert, A. Odermatt, N. Huber, Computation of thickness and mechanical properties of interconnected structures: Accuracy, deviations, and approaches for correction, Front. Mater. 6 (327) (2019).
[43] T. Krekeler, A.V. Straßer, M. Graf, K. Wang, C. Hartig, M. Ritter, J. Weissmüller, Silver-rich clusters in nanoporous gold, Mater. Res. Lett. 5 (2017) 314–321.
[44] M. Haensch, M. Graf, W. Wang, A. Nefedov, C. Wöll, J. Weissmüller, G. Wittstock, Thermally driven Ag–Au compositional changes at the ligament surface in nanoporous gold: Implications for electrocatalytic applications, ACS Appl. Nano Mater. 3 (3) (2020) 2197–2206.
[45] C.A. Schneider, W.S. Rasband, K.W. Eliceiri, NIH Image to ImageJ: 25 years of image analysis, Nat. Methods 9 (7) (2012) 671–675.
[46] D.W. Scott, On optimal and data-based histograms, Biometrika 66 (3) (1979) 605–610.
[47] R. Stine, in: J. Fox, J.S. Long (Eds.), Modern methods of data analysis, Sage, London, 1990, pp. 325–373.
[48] G.H. Hardy, J.E. Littlewood, G. Pólya, Inequalities, Cambridge university press, London, 1934, pp. 43–44.
[49] L.-Z. Liu, X.-L. Ye, H.-J. Jin, Interpreting anomalous low-strength and low-stiffness of nanoporous gold: Quantification of network connectivity, Acta Mater. 118 (2016) 77–87.
[50] Y. Li, B.-N.D. Ngô, J. Markmann, J. Weissmüller, Topology evolution during coarsening of nanoscale metal network structures, Phys. Rev. Mater. 3 (7) (2019) 076001.
[51] C. Richert, N. Huber, Skeletonization, geometrical analysis, and finite element modeling of nanoporous gold based on 3D tomography data, Metals 8 (4) (2018) 282.
[52] G. Brug, M. Sluyters-Rehbach, J. Sluyters, A. Hemelin, The kinetics of the reduction of protons at polycrystalline and monocrystalline gold electrodes, J. Electroanal. Chem. Interfacial Electrochem. 181 (1–2) (1984) 245–266.
[53] A. Hamelin, L. Stoicoviciu, F. Silva, The temperature dependence of the double-layer properties of gold faces in perchloric acid solutions: Part I. the (210) gold face, J. Electroanal. Chem. Interfacial Electrochem. 229 (1–2) (1987) 107–124.
[54] P.S. Germain, W.G. Pell, B.E. Conway, Evaluation and origins of the difference between double-layer capacitance behaviour at Au-metal and oxidized Au surfaces, Electrochim. Acta 49 (11) (2004) 1775–1788.